Core–Shell Structured Silicon Nanoparticles@TiO_{2-x}/Carbon Mesoporous Microfiber Composite as a Safe and High-Performance Lithium-Ion Battery Anode

Goojin Jeong,[†,⊥,*] Jae-Geun Kim,[‡,⊥] Min-Sik Park,[†] Minsu Seo,[†] Soo Min Hwang,[‡] Young-Ugk Kim,[§] Young-Jun Kim,[†] Jung Ho Kim,[‡,*] and Shi Xue Dou[‡]

[†]Advanced Batteries Research Center, Korea Electronics Technology Institute, Seongnam 463-816, Republic of Korea, [‡]Institute for Superconducting and Electronic Materials, University of Wollongong, North Wollongong NSW 2500, Australia, and [§]Corporate R&D Center, Samsung SDI, Suwon 443-803, Republic of Korea. [⊥]G.J. and J.-G.K. contributed equally to this work.

ABSTRACT A core–shell structured Si nanoparticles@TiO_{2-x}/C mesoporous microfiber composite has been synthesized by an electrospinning method. The core–shell composite exhibits high reversible capacity, excellent rate capability, and improved cycle performance as an anode material for Li-ion batteries. Furthermore, it shows remarkable suppression of exothermic behavior, which can prevent possible thermal runaway and safety problems of the cells. The improved electrochemical and thermal properties are ascribed to the mechanically, electrically, and thermally robust shell structure of the TiO_{2-x}/C nanocomposite encapsulating the Si nanoparticles, which is suggested as a promising material architecture for a safe and reliable Si-based Li-ion battery of high energy density.

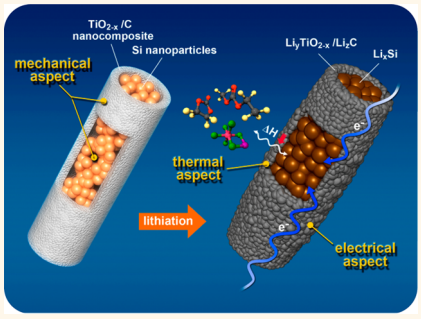

KEYWORDS: silicon · nonstoichiometric TiO_2 · core–shell · volume expansion · conductivity · thermal property · lithium-ion battery

Lithium-ion batteries (LIBs) have been employed successfully in various small electronic devices for the past two decades, and the types of applications are currently expanding to include electric vehicles and large electric power storage units. In order to be implemented in these emerging markets, novel materials for anodes and cathodes as well as electrolytes need to be developed to achieve high energy density, high power, and safe lithium rechargeable batteries. Considerable attention has been paid to the use of Si-based anode materials for LIBs because they theoretically possess much higher capacity than graphite (3590 mAh g^{-1} for $Li_{3.75}Si$ and 372 mAh g^{-1} for LiC_6). Although the Si anodes deliver high specific capacity, they suffer from volume expansion, which leads to mechanical degradation of the Si materials during repeated cycling and thereby poor cycle performance.[1,2] Research and development of Si-based anodes has been accelerated with the advance of nanotechnology since Fuji announced amorphous tin composite oxide (ATCO) as an anode material in 1997.[3] Nanostructured Si-based anode materials have been known to facilitate stain/stress relaxation and also shorten the Li diffusion length, so that an improved capacity, rate capability, and cycle performance can be achieved.[4] Several types of Si nanomaterials, such as active/inactive nanocomposites,[5] nanosized particles with various morphologies,[6,7] and meso/macroporous materials,[8–11] have been explored. Some of them are deployed in commercial LIB, as found in Hitachi Maxell's cell where a SiO material was adopted as part of the anode composition.[12] The content of SiO in the anode was, however, limited under 10 wt % because of the intrinsic volume expansion and the low initial Coulombic efficiency as well as the unguaranteed safety issue with increasing energy density of the cell. Thus, Si-based anode materials

* Address correspondence to gjeong@keti.re.kr, jhk@uow.edu.au.

Received for review January 16, 2014 and accepted February 19, 2014.

Published online February 19, 2014
10.1021/nn500278q

should be further researched and developed for a competitively upgraded Si-based LIB having higher energy density, compared with the currently used graphite-based LIB.

High capacity and long cycle life have to be given priority in development of Si-based anode materials. However, concerns on the safety issue with the increased high energy density of a Si-employed LIB must be addressed before its practical application. Generally, the lithiated anode material is thermodynamically unstable and reacts exothermally with an electrolyte at an elevated temperature.[13] Unlike graphite anode material, however, only a few studies on the thermal properties of lithiated Si-based anode have been reported.[14−16] Previously, our group reported the thermal properties of Si and SiO materials.[17] The large heat generation including a severe exotherm in the 300−400 °C range was observed for the Si-based materials, approximately 3-fold larger than the heat generation of graphite. The undesirable exothermic behavior was still observed for carbon-coated Si where the carbon has been regarded as a typical material of choice for improving the electrochemical performance of LIB electrode materials. Consequently, the larger heat generation in Si-based anodes is considered a potential risk factor inducing violent explosion of the battery under hazardous conditions. To suppress the undesirable exotherm, we replaced the carbon coat with a TiO_2 layer and, finally, could thus stabilize the thermal behavior of the SiO. However, the electrochemical performance was not much improved, probably due to the low electrical conductivity, so further development is necessary to achieve well-balanced cell performance for practical applications.

Herein, we report another promising material architecture for a high-performance and safety-reliable Si-based anode material, such as a core−shell structured Si nanoparticles@TiO_{2-x}/C mesoporous microfiber composite, which has the features of a mechanically, electrically, and thermally robust microstructure. For a core−shell structured Si nanoparticle@TiO_{2-x}/C mesoporous microfiber composite, the expected function is three-fold as follows (Scheme 1): (i) Encapsulation of Si nanoparticles inside a one-dimensional hollow and rigid TiO_{2-x}/C composite scaffold, with reserved void space therein, can suppress the disintegration of the Si nanoparticles undergoing repeated volume change during cycling and thereby improve the cycle performance (mechanically robust structure). (ii) Oxygen-deficient titania (TiO_{2-x}) and carbon as the shell components can provide an enhanced electrical pathway of high conductivity for the electrochemical reaction between Li and Si, thereby improving the cell performance. Oxygen-deficient TiO_2 has been intensively studied for various application fields owing to its narrower band gap enabling relatively high electrical conductivity.[18−25] For a battery material, a black TiO_2, showing oxygen-deficiency, has showed promising anode performance compared with a typical white TiO_2, by resolving the problem of the initial low electrical conductivity.[22] An oxygen-deficient TiO_2 as well as the *in situ* formed Li_xTiO_2 phase[26,27] during lithiation can support a favorable electrical environment with carbon in the shell structure (electrically robust structure). (iii) When the TiO_2 is introduced as a main shell component, enhanced thermal stability of the Si composite can also be obtained.[17] The reason is that the TiO_2 shell is anticipated to act as a physical/chemical interfacial barrier, retarding exothermic reaction between the highly lithiated Si phase and the electrolyte solution, combined with the intrinsically stable thermal property of the TiO_2 itself (thermally robust structure).[28,29] From the above expectations, a core−shell structured Si nanoparticles@TiO_{2-x}/C mesoporous microfiber composite can thus be a promising material architecture for a safe and high-performance Si-based LIB.

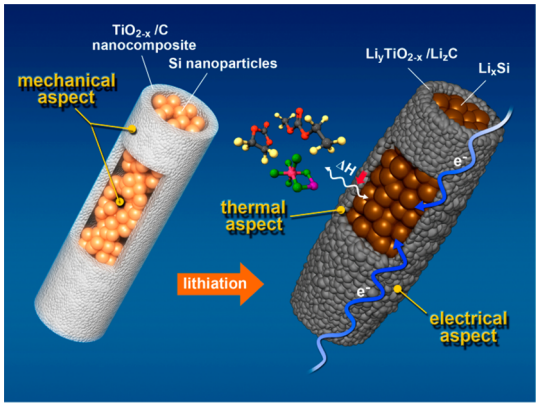

Scheme 1. Schematic illustration of a core−shell structured Si nanoparticles@TiO_{2-x}/C mesoporous microfiber composite as an anode material for Li-ion batteries, which has the features of a mechanically, electrically, and thermally robust architecture. The molecules expressed with ball and stick model indicate EMC, EC, and $LiPF_6$ in the electrolyte solution (counterclockwise from top) and the ΔH means an exothermic enthalpy in the reaction between Li_xSi and electrolyte.

RESULTS AND DISCUSSION

A core−shell structured Si nanoparticles@TiO_{2-x}/C mesoporous microfiber composite (hereafter denoted as SiNPs@T/C) was prepared by a dual-nozzle electrospinning method which is facile and smart for synthesis of functional fibers.[30] Si nanoparticles dispersed in a poly(methyl methacrylate) (PMMA) solution were injected into the core channel of the nozzle, whereas titanium(IV) isopropoxide dissolved in a PMMA solution was injected into the shell channel of the nozzle. After the single electrospinning step, the product was heated to 800 °C to obtain TiO_{2-x}/C nanocomposite. Details of materials and experimental methods are described in the Experimental Details. The morphology and crystalline microstructure of the electrospun fibers

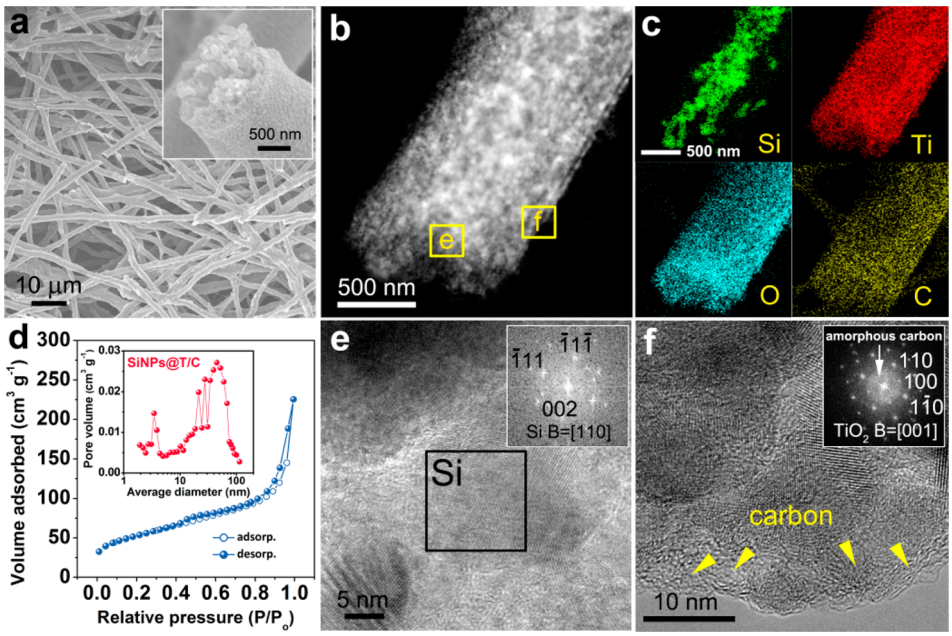

Figure 1. (a) SEM images of the electrospun SiNPs@T/C. (b) HAADF STEM image of SiNPs@T/C and (c) EDS elemental mapping for silicon, titanium, oxygen, and carbon. (d) N_2 adsorption/desorption isotherm and the pore size distribution (inset) of SiNPs@T/C: the BET surface area is 163 m^2 g^{-1}, and the average pore volume is 0.33 cm^3 g^{-1}. HRTEM images and the corresponding FFTs (inset) for (e) core region and (f) shell region of SiNPs@T/C: the observed crystallites in the HRTEM image correspond to rutile TiO_2, and the amorphous regions correspond to carbon.

were directly confirmed by scanning electron microscopy (SEM), transmission electron microscopy (TEM), scanning TEM (STEM), and X-ray diffraction (XRD). As shown in Figure 1a, the electrospun fibers revealed the randomly aligned microfibers having average diameters of ~2 μm and length extending to several tens of micrometers. The core–shell structure was observed by SEM (the inset in Figure 1a) and was further clearly confirmed by the high-angle annular dark-field (HAADF) STEM images and the corresponding energy-dispersive spectroscopy (EDS) elemental mapping for Si, Ti, O, and C (Figure 1b,c). The core region was full of Si nanoparticles (50–100 nm diameter for each Si nanoparticle) with reserved void space that may be produced by unzipping of PMMA[31,32] used in the solution for the core channel in the dual-nozzle electrospinning. The outer-shell section composed of Ti, O, and C showed a thickness of 200–300 nm and also porous characteristics. The pore structure of the electrospun fibers was further investigated by nitrogen sorption measurement (Figure 1d). The N_2 adsorption/desorption isotherm indicates the characteristics of mesoporous materials. The Brunauer–Emmett–Teller (BET) surface area was 163 m^2 g^{-1}, and the average pore volume of Barrett–Joyner–Halenda (BJH) was 0.33 cm^3 g^{-1}, which strongly confirmed the mesoporous structure of the electrospun fibers. The identified porosity may be helpful in accessing the electrolyte solution and to accommodate the volume expansion of the Si nanoparticles when the microfiber is used as an anode material for LIBs.[8,9] The phase information corresponding to the core and shell region was identified by the high-resolution TEM (HRTEM) image and the corresponding fast Fourier transform (FFT). The HRTEM images and FFTs indicated the crystalline Si (Figure 1e) for the core section, the nanocomposite of rutile TiO_2 and amorphous carbon for the shell (Figure 1f), which conclusively proved that crystalline Si nanoparticles were encapsulated by a TiO_2/C nanocomposite in the electrospun fibrous composite. The XRD and Raman spectroscopy results (see the Supporting Information, Figures S1 and S2) supported the above-stated microstructure of the SiNPs@T/C. The presence of carbon in the shell of the SiNPs@T/C deserves mention. The content of carbon in the TiO_2/C shell was about 14 wt %, measured by thermogravimetric analysis (Supporting Information, Figure S3). The carbon is considered to originate from the PMMA used in the solution for the shell channel in the dual-nozzle electrospinning. Generally, PMMA leaves no residue after pyrolysis even in inert atmosphere.[31,33] In certain cases, however, PMMA can be carbonized.[34,35] According to the literature, we also speculate that TiO_2 gel in the PMMA partly terminates the chain degradation of PMMA by intercepting some of the free radicals during depolymerization, which leads to the formation of carbon in our SiNPs@T/C material.

As shown in Figure 2a, the SiNPs@T/C has dark-green color. Many reports have discussed coloration of TiO_2 in relation with the electronic structure.[18–25,36,37] The coloration in our sample also implied the presence of nonstoichiometric TiO_2, and we further investigated the electronic structure of the TiO_2 in the SiNPs@T/C and the effect on electrical conductivity. Figure 2a

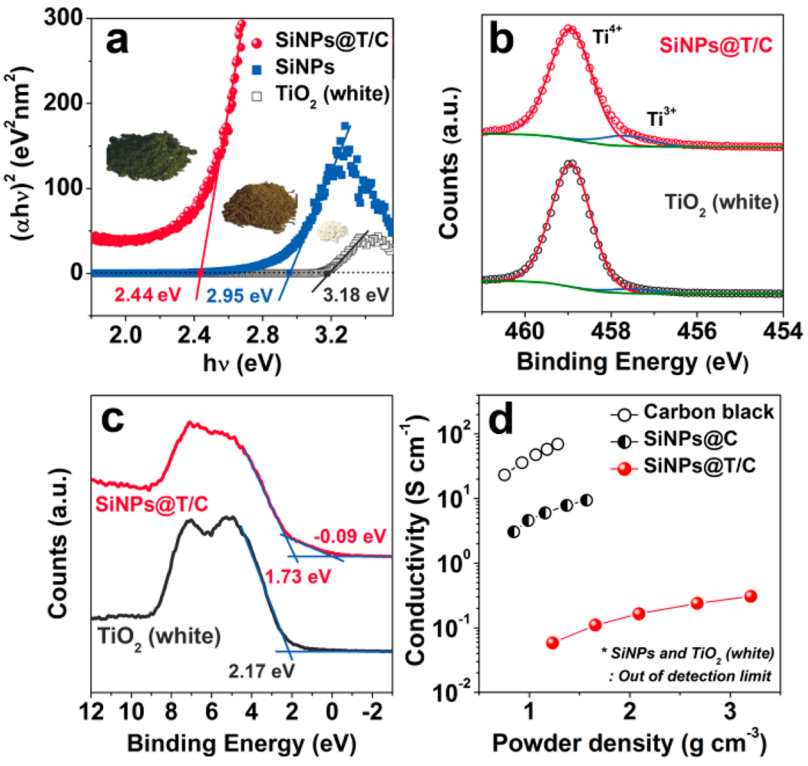

Figure 2. (a) Tauc plots representing band gap energy of SiNPs@T/C, SiNPs, and white TiO_2, including digital camera images of the powders showing the colors: dark-green for SiNPs@T/C, brown for SiNPs, and white for TiO_2. The band gap energy of SiNPs is higher than 1.1 eV known as a typical value for silicon because of the native silicon oxide and/or nanosize effect of SiNPs.[49] (b) Ti $2p_{3/2}$ XPS spectra for SiNPs@T/C and white TiO_2. The measured spectra were deconvoluted by TiO_2 (+4) and Ti_2O_3 (+3). (c) Valence band XPS spectra of SiNPs@T/C and white TiO_2. Of the two main bands in the valence band, the low binding energy state (5−6 eV) is assigned to O 2p−Ti 4sp π bonding, and the electronic band at high binding energy (7−8 eV) is predominantly due to O 2p−Ti 3d σ bonding.[19] Thin blue lines show the linear extrapolation of the curves used for deriving the band edge position of the samples. (d) Electrical conductivities of SiNPs@T/C, SiNPs@C, and carbon black powders.

presents the Tauc plot[38] derived from the diffusive reflectance UV−vis spectroscopy analysis for the SiNPs@T/C. It revealed that the optical band gap of SiNPs@T/C was 2.44 eV, whereas the band gap of white TiO_2 as a reference was 3.18 eV. In the latter, the SiNPs@T/C exhibited a broad absorption extending to the near-infrared (NIR) region of the spectrum (Supporting Information, Figure S4), which gave it a dark-green coloration. To clarify the physical origin of the visible−NIR light absorption of the SiNPs@T/C, its electronic properties were investigated by using X-ray photoelectron spectroscopy (XPS) measurement. Although both SiNPs@T/C and white TiO_2 showed typical Ti 2p core-level XPS spectra with Ti^{4+} characteristics (Ti $2p_{3/2}$ peak at 459.0 eV of binding energy), SiNPs@T/C also exhibited a shoulder near 457.7 eV, which is characteristic of Ti^{3+} (Figure 2b).[23] The ratio of Ti^{3+} to Ti^{4+} was calculated to be 9.7/90.3, assumed to be $TiO_{1.952}$. According to the literature,[36,39] defects can be generated in TiO_2 structure in inert atmosphere due to partial oxygen loss leading to reduction and vacancy generation and the reduction to Ti^{3+} strongly influences the density of the state distribution. Figure 2c exhibits valence band (VB) XPS of SiNPs@T/C and white TiO_2. A white TiO_2 displayed the VB maximum edge at 2.17 eV, and since the optical band gap is 3.18 eV from the above UV−vis measurement, the conduction band (CB) minimum will occur at −1.01 eV. On the other hand, VB XPS of SiNPs@T/C showed notable differences: the main absorption onset was located at 1.73 eV, whereas the maximum energy associated with the band tail blue-shifted further toward the vacuum level at about −0.09 eV. Chen *et al.*[18] reported a substantial shift (2.18 eV) of the VB maximum edge for hydrogenated black TiO_2 nanoparticles, and Naldoni *et al.*[20] also presented very similar VB spectra for both white and black TiO_2. In our case, the TiO_{2-x} of the shell component in the SiNPs@T/C also has a distinctive density of states (DOS) structure. If for the TiO_{2-x} the same CB energy shape is assumed as for white TiO_2 reference, a remarkable narrowing in the band gap (0.62 eV) can be observed (Supporting Information, Figure S5). Therefore, electronic transition from tailed VB to CB in the narrowing band gap, which is induced by the presence of Ti^{3+}, is responsible for the TiO_{2-x} shell in the SiNPs@T/C. As expected from the reduction in the band gap energy of TiO_2 and the presence of carbon in the shell of the SiNPs@T/C, the electrical conductivity of the SiNPs@T/C was found to be relatively high, 3×10^{-1} S cm^{-1} (Figure 2d). Although the value is

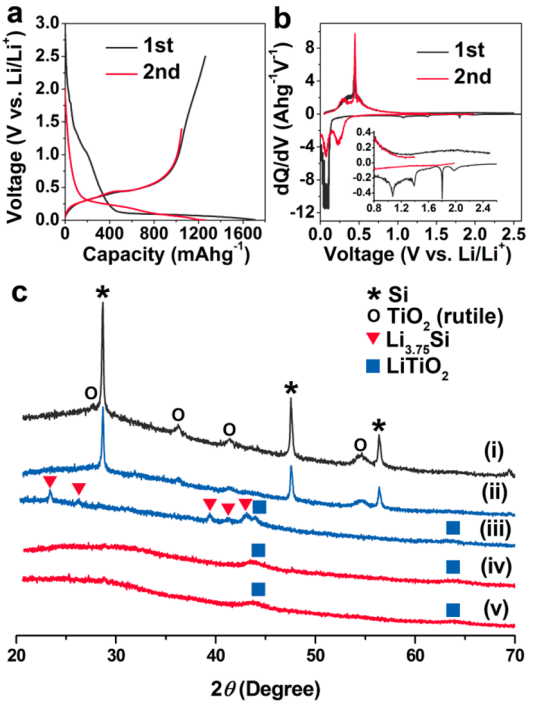

Figure 3. (a) Galvanostatic voltage profiles and (b) corresponding DCPs of SiNPs@T/C half-cell during the first and second cycles. The inset in (b) shows the enlarged DCPs in the voltage region of 0.8−2.5 V. (c) Evolution of the XRD patterns of SiNPs@T/C during the first cycle; (i) the fresh electrode, (ii) discharged by 1.0 V (*vs* Li/Li$^+$), (iii) discharged by 0.005 V, (iv) charged by 1.4 V, and (v) charged by 2.5 V.

lower than those of carbon black and SiNPs@C (we also prepared a core−shell structured Si nanoparticles@carbon fibrous composite for comparison, denoted as SiNPs@C, which was already reported as a promising anode material[32,40]), it is much higher than those of white TiO_2 and Si nanoparticles: the electrical conductivities of white TiO_2 and Si nanoparticles could not be measured in this study because of their too low conductivities. From references 41 and 42, the known electrical conductivities of rutile TiO_2 (white) and Si nanoparticles are 7×10^{-7} and 10^{-8}−10^{-7} S cm^{-1}, respectively. Consequently, the significantly increased electrical conductivity of SiNPs@T/C appears to enhance the electrochemical performance of an LIB anode material.

To investigate electrochemical performance of the SiNPs@T/C as an anode material for LIBs, we constructed the 2032 coin-type half-cell and evaluated it in several electrochemical tests. Figure 3a shows the first and second voltage profiles of the SiNPs@T/C anode material. The discharge (lithiation) and charge (delithiation) capacities were 1710 and 1260 mAh g^{-1}, respectively. The initial Coulombic efficiency (ICE) corresponded to 74%, which exceeded that of the pure Si nanoparticle anode (68%). It implies that the well-integrated core−shell structure of the SiNPs@T/C suppresses the possible structural collapse produced by the volume change of Si, enhancing reversibility of the Li−Si electrochemical reaction. The preservation of the core−shell structure and the expansion ratio of the electrode after the first lithiation were verified by SEM images (Supporting Information, Figure S6). The overall fibrous morphology was clearly maintained, and the expansion ratio was ∼57%, which is comparable to the already reported advanced Si anode materials, such as a Si nanotube (∼54%)[43] and an urchin-like Si/SiO_x nanocomposite (∼50%).[44]

It is important to further check whether high capacity of an anode material is really increasing the energy density of the full-cell battery where the anode is employed. The reason is that not only the reversible capacity of an anode but also the ICE, electrode density (especially, lithiated, *i.e.*, expanded state in the case of Li alloy anode), and operational voltage of the full-cell are critical factors determining the energy density of a full-cell battery. To compare the volumetric energy density of the SiNPs@T/C-employed full-cell with a graphite-employed one, we established a single full-cell configuration where $LiCoO_2$ (LCO) was applied as a cathode. As presented in the Supporting Information, Figure S7 and Table S1, the SiNPs@T/C−LCO system revealed ∼8% higher energy density than that of the graphite−LCO. For a more competitive energy density to replace a graphite system, however, the ICE and the volume expansion as well as capacity need to be further perfected.

As indicated in the differential capacity plot (DCP) of the SiNPs@T/C (Figure 3b), the main discharge/charge reaction is based on alloying/dealloying between Li and Si. Besides the Li−Si electrochemistry, the rutile TiO_{2-x} as a shell structure in the SiNPs@T/C also takes part in the initial electrochemical reaction. As well-noted in the literature,[45] a nanostructured rutile TiO_2 is one of the candidates for an anode material in LIBs. Li ion can insert into TiO_2 during the initial discharge process at about 1.7−1.8 V, leading to the formation of $Li_{0.5}TiO_2$. It has been well-known that the *in situ* formed Li_xTiO_2 also has an enhanced electrical conductivity due to the existence of Ti^{3+},[26,27] as well as TiO_{2-x}, and thus can also be advantageous for electrical pathways similar to the traditional carbon coat on electrode materials for LIBs. Several DCP peaks (inset in Figure 3b) could be observed in the potential range of 0.8−2.4 V in the initial discharge process of the SiNPs@T/C. A peak at 1.8 V corresponds to Li-ion insertion into the TiO_{2-x}, and other DCP peaks are related to electrolyte decomposition on the surface of SiNPs@T/C. The phase evolution of the rutile TiO_{2-x} during insertion/extraction of the Li ion can be identified by *ex situ* XRD analysis, as shown in Figure 3c. When a SiNPs@T/C was lithiated by 1.0 V (*vs* Li/Li$^+$), the corresponding XRD pattern showed no change *versus* the fresh electrode. It indicates that the lithiated SiNPs@T/C, more specifically, the lithiated TiO_{2-x} of the shell component in the composite, initially retains a rutile-type structure upon

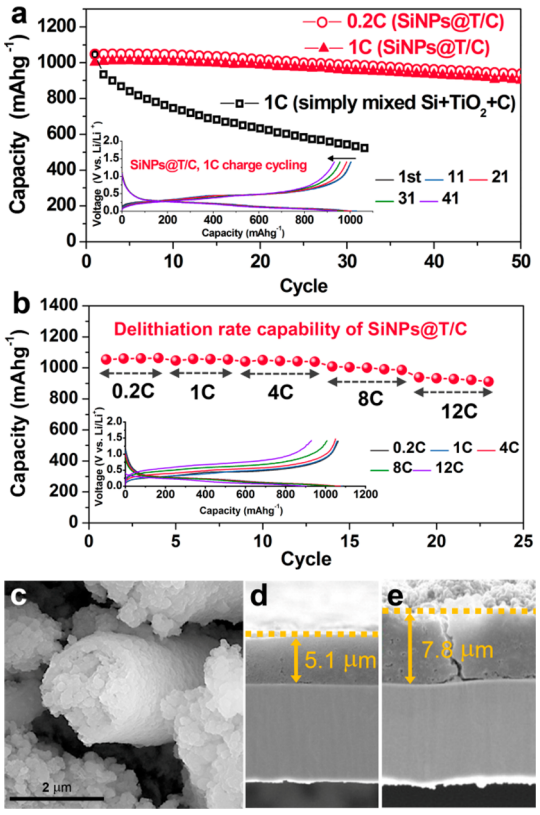

Figure 4. (a) Capacity retention of SiNPs@T/C during cycling and the corresponding voltage profiles (inset). (b) Delithiation rate capability of SiNPs@T/C and the corresponding voltage profiles (inset). For the cycle and rate capability tests, lithiation current density was fixed as 0.2C/0.1C (5 mV) CCCV mode. (c) SEM image of SiNPs@T/C after 50 cycles (lithiated state). The cross-sectional SEM images of SiNPs@T/C electrode (d) before cycling and (e) after 50 cycles (lithiated state). The observed expansion ratio was ~53%.

lithiation. Further lithiation down to 0.005 V leads to the appearance of $LiTiO_2$ phase of cubic rock-salt structure (2θ = 43.8 and 63.5°, JCPDS #16-0223) in addition to the $Li_{3.75}Si$ alloy phase formed by lithiation of Si nanoparticles of the core component. On the reverse charging process, the $LiTiO_2$ phase still remains even in the fully delithiated state, indicating the irreversible trapping of Li in TiO_{2-x}. The above observed phase evolution of rutile TiO_{2-x} and Si in the first cycle matches well to the previous results in the literature.[27,46−48] Although the irreversible $LiTiO_2$ phase causes the low Coulombic efficiency in the first cycle, it has a positive effect, as previously mentioned, on the following cycle or rate performance of the SiNPs@T/C by providing an electrical scaffold structure having an enhanced electrical conductivity.

Figure 4a exhibits the cycling performance of the SiNPs@T/C. For comparison, the simply mixed Si−TiO_2−C electrode in the same weight ratio with the SiNPs@T/C electrode (the Si content in the SiNPs@T/C is ~43%, analyzed by STEM-EDS; see the Supporting Information, Table S2) is also tested.

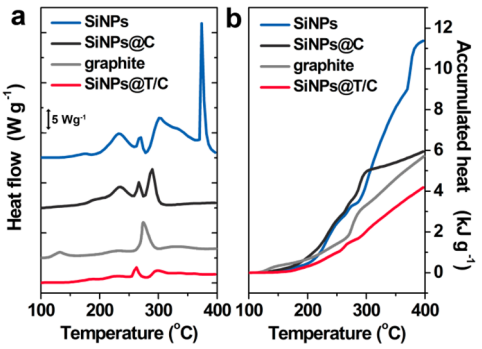

Figure 5. (a) DSC curves and (b) corresponding accumulated heat curves of SiNPs@T/C, SiNPs@C, SiNPs, and graphite anode materials. All samples were fully lithiated (discharged to 5 mV) for the first cycle.

When cycled at 0.2C, the SiNPs@T/C displayed good capacity retention (*i.e.*, 90% of the initial capacity after 50 cycles), showing obviously a superior performance to the simply mixed Si−TiO_2−C. When cycled at a higher current density of 1C, the SiNPs@T/C still delivered excellent cycling performance where the capacity and its retention were almost the same as the performance at 0.2C. The SiNPs@T/C also exhibited outstanding rate capability (Figure 4b), where a high capacity of 939 mAh g^{-1} is observed even at a significantly high current density of 12C (12 A g^{-1}), that is, 89% of the initial capacity at 0.2C. These outstanding electrochemical performances indicate that the fibrous core−shell structure of the SiNPs@T/C resolves some serious issues in Si-based anode materials, such as collapse of electrical network in the electrode due to the mechanical degradation by volume change of the Si. The mechanically robust TiO_{2-x}/C shell can suppress the disintegration of the Si nanoparticles in the SiNPs@T/C composite. Also, the initial TiO_{2-x} and the *in situ* formed Li_xTiO_2 phase in the shell structure promote the electron/Li-ion path in the SiNPs@T/C and thereby improve the electrochemical performance of the SiNPs@T/C. Figure 4c−e shows the SEM images of the SiNPs@T/C particle and the cross section of the SiNPs@T/C electrode after 50 cycles. The fibrous core−shell structure free of a significant collapse can be clearly observed even after 50 cycles. Also, the volume expansion after the 50th discharge is still ~53%, which is almost the same as the value after the first discharge step (see again Supporting Information, Figure S6), indicating stable volume change during cycling.

In addition to the electrochemical performance, we also investigated the thermal property of the lithiated SiNPs@T/C, focusing on the effect of the TiO_{2-x} shell structure. Figure 5 shows differential scanning calorimetry (DSC) scans of the different lithiated anode materials including the SiNPs@T/C. All the measurements were performed at 100% SOC (state of charge) in the presence of the entrapped electrolyte. Compared with the graphite which showed a relatively low exotherm

in the overall temperature range (5.7 kJ g^{-1}), the bare Si nanoparticles (SiNPs) exhibited larger exothermic enthalpy (11.4 kJ g^{-1}), especially with an abrupt exothermic peak in the 350−400 °C range. Although a more systematic clarification of the DSC behavior of the bare SiNPs, beyond the scope of this paper, is required, the larger exothermic enthalpy including the abrupt exotherm above the 350 °C is regarded as an intense reaction between the highly lithiated Li_xSi and the electrolyte solution as previously reported.[17] The large exothermic behavior of Si material can be problematic with respect to safety concerns in the development of a Si-based LIB because the thermal behavior can lead to a cell explosion under extreme conditions, such as penetration or high-temperature exposure. For a more specific investigation of the thermal property of the SiNPs@T/C, we also examined the thermal property of the SiNPs@C material[40] because the carbon coating or carbon composite for a Si anode has been regarded as the most effective way for enhancing the electrochemical performance. The SiNPs@C exhibited less exothermic enthalpy in the overall temperature range (6.0 kJ g^{-1}) than the bare SiNPs. However, the heat generation in the 150−300 °C range was still the same as for bare SiNPs, which indicates that the carbon-shell structure cannot perfectly suppress the intensive exothermic reaction between Li_xSi and the electrolyte.

Unlike the bare SiNPs and SiNPs@C, the SiNPs@T/C exhibited a significantly reduced exotherm in the overall temperature range (4.2 kJ g^{-1}), which is comparable to graphite. This remarkable thermal stabilization is considered to originate from the TiO_{2-x} shell structure. The shell which is mainly composed of TiO_{2-x} possibly retards the intensive thermal reaction between the highly lithiated Si and the electrolyte solution. In addition, the well-noted thermal stability of lithiated TiO_2 and its solid electrolyte interphase are considered to be other possible reasons for the suppressed exothermic reaction in the SiNPs@T/C. The quantitative relationship between the DSC results and the actual safety characteristics of LIB is not linearly dependent. The present results, however, suggest that the thermal stability of the fully lithiated Li_xSi phase is definitely improved when the Si nanoparticles are encapsulated by TiO_{2-x}.

CONCLUSION

Achievement of the high energy density and the long cycle life of a Si-based LIB should be accompanied with guaranteed safety. Here we have presented the synthesis and characterization of a core−shell structured Si nanoparticles@TiO_{2-x}/C mesoporous microfiber composite as an anode for LIBs and the analysis of its electrochemical and thermal properties. The microstructure was identified by various analytical methods as a core−shell fibrous composite consisting of a porous assembly of Si nanoparticles as the core and the mesoporous wall of rutile TiO_{2-x}/C nanocomposite as the shell structure. The SiNPs@T/C exhibited high reversible capacity, excellent rate capability, and good cycle performance. Furthermore, it showed remarkable suppression of exothermic behavior in comparison with bare SiNPs and a SiNPs@C fibrous composite. The stabilized thermal property can prevent possible thermal runaway and safety problems of a Si-based LIB. The improved electrochemical and thermal properties are ascribed to the mechanically, electrically, and thermally robust shell structure of the TiO_{2-x}/C nanocomposite encapsulating the Si nanoparticles. In many efforts for the commercialization of Si-based LIBs, the core−shell structured Si nanoparticles@TiO_{2-x}/C mesoporous microfiber composite can thus offer a promising material architecture for a safe and reliable Si-based LIB of high energy density.

EXPERIMENTAL DETAILS

Preparation of SiNPs@T/C. For the core polymer solution, 0.5 g of Si nanoparticles (Nanostructured & Amorphous Materials, 50−70 nm) was dispersed in 10 mL of *N*,*N*-dimethylformamide (DMF, Simga-Aldrich), and 1.045 g of poly(methyl methacrylate) (PMMA, M_w = 350 000, Simga-Aldrich) was dissolved in dispersed Si solution by stirring at 90 °C for at least 8 h. On the other hand, the shell solution was prepared by dissolving 1.567 g of PMMA in 10 mL of DMF and 5 mL of acetic acid (Simga-Aldrich). After dissolving over 8 h, 2 mL of titanium(IV) isopropoxide (TTIP, Simga-Aldrich) was added in PMMA solution, followed by magnetic stirring for 1 h. The brown core polymer solution was immediately loaded into a plastic syringe equipped with the inner channel of a dual nozzle (NNC-DN-1723, NanoNC, Korea), which has a 23-gauge inner needle (0.63 mm o.d., 0.33 mm i.d.) and a 17-gauge outer needle (1.47 mm o.d., 1.07 mm i.d.). The light yellow transparent shell polymer solution was loaded into other plastic syringe which was connected to the outer channel at the dual nozzle. The dual nozzle was connected to a high voltage supply, and the feeding rate of the core and shell solutions was set at 1.5 and 3.0 mL h^{-1}, respectively. A distance of 21.5 cm and voltage of 15 kV were maintained between the tip of the dual nozzle and a drum collector. After the electrospinning, the electrospun nanofibers were peeled off from the drum collector. Finally, the electrospun nanofibers were heat-treated at 800 °C for 3 h in nitrogen atmosphere.

Characterization Methods. The morphology, microstructure, and compositional analysis of the synthesized materials were examined using a field emission scanning electron microscope (FESEM, JEOL JSM-7000F), a high-resolution transmission electron microscopy (HRTEM, ARM-200F, JEOL) having a probe C_s aberration corrector (CEOS GmbH) and an energy-dispersive spectroscopy system that was attached to the TEM system. The crystalline structure analysis of the synthesized materials was performed using an Empyrean diffractometer (PANalytical) equipped with monochromated Cu Kα radiation (λ = 1.54056 Å). For *ex situ* XRD analyses of the discharged or charged electrode, a gastight sample holder filled with Ar and covered with a polyimide (Kapton) tape was used. After the cell reacted up to a certain level, the electrode was carefully disassembled from the cell and then rinsed with dimethyl carbonate (DMC) in an Ar-filled glovebox to remove residual electrolyte.

The electrodes were then dried under vacuum for 3 h and transferred to the *ex situ* XRD holder. The morphology change and cross-sectional image of electrodes after cycling was analyzed by FESEM. Similar to the *ex situ* XRD analysis, the cells were carefully disassembled and the electrodes were subsequently rinsed with DMC. They were then dried under vacuum for 3 h and transferred to the chamber of SEM equipment. The chemical binding state and electronic structure were examined by X-ray photoelectron spectroscopy (XPS, Thermo Scientific Sigma Probe) with Al Kα X-rays. Diffuse reflectance UV−vis spectra of powders were measured on JASCO spectrophotometer (V-670, Japan), and all the samples were measured under ambient conditions. The surface area and pore volume of the synthesized materials were measured by Brunauer−Emmett−Teller (BET) and Barrett−Joyner−Halenda (BJH) methods, respectively, using a surface area and porosimetry analyzer (TristarII 3020, Micromeritics). The electrical conductivity of powder-type samples was measured by a direct volt-ampere method (MCP-PD51, Mitsubishi Chemical Analytech) in which a sample was pressurized and contacted with a four-point probe. Differential scanning calorimetry (DSC) was performed using a Model Star system (Mettler Toledo), and the lithiated electrode samples were prepared by discharging the 2032 coin half-cells to 0.005 V at a slow rate of 60 mA g^{-1}. These cells were disassembled in a dry room (the dew point of less than −60 °C), and the electrodes were rinsed with DMC and dried under vacuum. Then, 1.5 mg of the electrode and 0.5 mg of fresh electrolyte solution were sealed in a high-pressure DSC pan. The heating rate and temperature range of the DSC tests were 5 °C min^{-1} and 25−400 °C, respectively.

Electrochemical Testing. The electrodes were prepared by coating copper foil substrates (thickness: 10 μm) with slurries containing the active material powders (80 wt %), carbon black (Super-P, 10 wt %), and poly(acrylic acid) (PAA, 10 wt %) dissolved in water. After coating, they were dried at 80 °C for 30 min in a convection oven to evaporate the water and then heat-treated at 120 °C for 6 h under vacuum. The electrodes were cut into disks (12 mm in diameter), in which the mass of the active material was approximately 1−3 mg. Then 2032 coin cells were assembled in a dry room that provided humidity at a dew point of less than −60 °C, using a polypropylene separator (Asahi Kasei Chemicals); 1 M $LiPF_6$ in a mixture of ethylene carbonate (EC) and ethyl methyl carbonate (EMC) (EC/EMC = 1/2 ratio) containing 20% fluoroethylene carbonate (FEC) as an electrolyte solution; and lithium foil (14 mm in diameter) as a counter-electrode. The assembled cells were aged overnight at room temperature and then electrochemically tested using a TOSCAT-3100U (Toyo System Co.) battery measurement system under the following protocols. The first cycle was operated at a constant current (CC) mode of 50 mA g^{-1} within a voltage window of 0.005−2.5 V *vs* Li/Li^+. The test protocol for cycle and rate performance was a constant current followed by a constant voltage (CCCV) mode for discharging (lithiation). In this mode, 0.2C (1C was set as 1100 mAg^{-1}) was used for the CC step and 0.005 V finished at 0.1C for the CV step. For charging (delithiation), the CC mode with various current densities was used and cut off by 1.4 V.

Conflict of Interest: The authors declare no competing financial interest.

Acknowledgment. Portions of this work were supported by an Automotive Australia 2020 project 1-111 and partly by the Energy Efficiency & Resources Program of KETEP (Project No. 20132020101700) grant funded by the Korea government Ministry of Trade, Industry & Energy (MOTIE) and partly by the IT R&D program of MKE/KEIT (10044962, Development of polymeric binder for silicon-based anode).

Note Added after ASAP Publication: After this paper was published ASAP on February 27, 2014, corrections were made to Figure 2 and to the first sentence in the Electrochemical Testing section. The corrected version was reposted March 7, 2014.

Supporting Information Available: XRD pattern, Raman spectra, UV−vis absorbance spectra, schematic DOS and SEM images after the first lithiation of the SiNPs@T/C, simulated voltage profile of the SiNPs@T/C−LCO full-cell compared with the graphite−LCO full-cell, summarized table and explanation for the full-cell simulation, an experimental detail for the synthesis of SiNPs@C and its characterization results, TGA curve of the TiO_{2-x}/C shell nanocomposite, and elemental composition of the SiNPs@T/C. This material is available free of charge *via* the Internet at http://pubs.acs.org.

REFERENCES AND NOTES

1. Szczech, J. R.; Jin, S. Nanostructured Silicon for High Capacity Lithium Battery Anodes. *Energy Environ. Sci.* **2011**, *4*, 56–72.
2. Jeong, G.; Kim, Y.-U.; Kim, H.; Kim, Y.-J.; Sohn, H.-J. Prospective Materials and Applications for Li Secondary Batteries. *Energy Environ. Sci.* **2011**, *4*, 1986–2002.
3. Idota, Y.; Kubota, T.; Matsufuji, A.; Maekawa, Y.; Miyasaka, T. Tin-Based Amorphous Oxide: A High-Capacity Lithium-Ion-Storage Material. *Science* **1997**, *276*, 1395–1397.
4. Wu, H.; Cui, Y. Designing Nanostructured Si Anodes for High Energy Lithium Ion Batteries. *Nano Today* **2012**, *7*, 414–429.
5. Jung, H.; Kim, Y.-U.; Sung, M.-S.; Hwa, Y.; Jeong, G.; Kim, G.-B.; Sohn, H.-J. Nanosize Si Anode Embedded in Super-Elastic Nitinol (Ni−Ti) Shape Memory Alloy Matrix for Li Rechargeable Batteries. *J. Mater. Chem.* **2011**, *21*, 11213–11216.
6. Chan, C. K.; Peng, H. L.; Liu, G.; McIlwrath, K.; Zhang, X. F.; Huggins, R. A.; Cui, Y. High-Performance Lithium Battery Anodes Using Silicon Nanowires. *Nat. Nanotechnol.* **2008**, *3*, 31–35.
7. Chen, X.; Gerasopoulos, K.; Guo, J.; Brown, A.; Wang, C.; Ghodssi, R.; Culver, J. N. Virus-Enabled Silicon Anode for Lithium-Ion Batteries. *ACS Nano* **2010**, *4*, 5366–5372.
8. Rong, J.; Masarapu, C.; Ni, J.; Zhang, Z.; Wei, B. Tandem Structure of Porous Silicon Film on Single-Walled Carbon Nanotube Macrofilms for Lithium-Ion Battery Applications. *ACS Nano* **2010**, *4*, 4683–4690.
9. Lee, J.-I.; Lee, K. T.; Cho, J.; Kim, J.; Choi, N.-S.; Park, S. Chemical-Assisted Thermal Disproportionation of Porous Silicon Monoxide into Silicon-Based Multicomponent Systems. *Angew. Chem., Int. Ed.* **2012**, *124*, 2821–2825.
10. Yamauchi, Y.; Suzuki, N.; Kimura, T. Formation of Mesoporous Oxide Fibers in Polycarbonate Confined Spaces. *Chem. Commun.* **2009**, *38*, 5689–5691.
11. Suzuki, N.; Kimura, T.; Yamauchi, Y. General Synthesis of Fibrous Mesoporous Metal Oxides in Polycarbonate Membrane. *J. Mater. Chem.* **2010**, *20*, 5294–5300.
12. LiB-Related Study, Program 10-11, Institute of Information Technology, Ltd., Japan, Aug. 2010.
13. Roth, E. P.; Doughty, D. H.; Franklin, J. DSC Investigation of Exothermic Reactions Occurring at Elevated Temperatures in Lithium-Ion Anodes Containing PVDF-Based Binders. *J. Power Sources* **2004**, *134*, 222–234 and references therein.
14. Wang, Y.; Dahn, J. R. Comparison of the Reactions between Li_xSi or $Li_{0.81}C_6$ and Nonaqueous Solvent or Electrolytes at Elevated Temperature. *J. Electrochem. Soc.* **2006**, *153*, A2188–A2191.
15. Zhao, L.; Han, S.-H.; Okada, S.; Na, B.-K.; Takeno, K.; Yamaki, J. Thermal Stability of Silicon Negative Electrode for Li-Ion Batteries. *J. Power Sources* **2012**, *203*, 78–83.
16. Park, Y.-S.; Lee, S.-M. Thermal Stability of Lithiated Silicon Anodes with Electrolyte. *Bull. Korean Chem. Soc.* **2011**, *32*, 145–148.
17. Jeong, G.; Kim, J.-H.; Kim, Y.-U.; Kim, Y.-J. Multifunctional TiO_2 Coating for a SiO Anode in Li-Ion Batteries. *J. Mater. Chem.* **2012**, *22*, 7999–8004.
18. Chen, X.; Liu, L.; Yu, P. Y.; Mao, S. S. Increasing Solar Absorption for Photocatalysis with Black Hydrogenated Titanium Dioxide Nanocrystals. *Science* **2011**, *331*, 746–750.
19. Tao, J.; Luttrell, T.; Batzill, M. A Two-Dimensional Phase of TiO_2 with a Reduced Bandgap. *Nat. Chem.* **2011**, *3*, 296–300.

20. Naldoni, A.; Allieta, M.; Santangelo, S.; Marelli, M.; Fabbri, F.; Cappelli, S.; Bianchi, C. L.; Psaro, R.; Dal Santo, V. Effect of Nature and Location of Defects on Bandgap Narrowing in Black TiO_2 Nanoparticles. *J. Am. Chem. Soc.* **2012**, *134*, 7600–7603.
21. Yang, C.; Wang, Z.; Lin, T.; Yin, H.; Lu, X.; Wan, D.; Xu, T.; Zheng, C.; Lin, J.; Huang, F.; *et al.* Core–Shell Nanostructured "Black" Rutile Titania as Excellent Catalyst for Hydrogen Production Enhanced by Sulfur Doping. *J. Am. Chem. Soc.* **2013**, *135*, 17831–17838.
22. Myung, S.-T.; Kikuchi, M.; Yoon, C. S.; Yashiro, H.; Kim, S.-J.; Sun, Y.-K.; Scrosati, B. Black Anatase Titania Enabling Ultra High Cycling Rates for Rechargeable Lithium Batteries. *Energy Environ. Sci.* **2013**, *6*, 2609–2614.
23. Xia, T.; Zhang, W.; Murowchick, J. B.; Liu, G.; Chen, X. A Facile Method To Improve the Photocatalytic and Lithium-Ion Rechargeable Battery Performance of TiO_2 Nanocrystals. *Adv. Energy Mater.* **2013**, *3*, 1516–1523.
24. Wang, Z.; Yang, C.; Lin, T.; Yin, H.; Chen, P.; Wan, D.; Xu, F.; Huang, F.; Lin, J.; Xie, X.; *et al.* H-Doped Black Titania with Very High Solar Absorption and Excellent Photocatalysis Enhanced by Localized Surface Plasmon Resonance. *Adv. Funct. Mater.* **2013**, *23*, 5444–5450.
25. Štengl, V.; Popelková, D.; Vláčil, P. TiO_2–Graphene Nanocomposite as High Performance Photocatalysts. *J. Phys. Chem. C* **2011**, *115*, 25209–25218.
26. Wang, Y.-Q.; Gu, L.; Guo, Y.-G.; Li, H.; He, X.-Q.; Tsukimoto, S.; Ikuhara, Y.; Wan, L.-J. Rutile-TiO_2 Nanocoating for High-Rate $Li_4Ti_5O_{12}$ Anode of Lithium-Ion Battery. *J. Am. Chem. Soc.* **2012**, *134*, 7874–7879.
27. Lotfabad, E. M.; Kalisvaart, P.; Cui, K.; Kohandehghan, A.; Kupsta, M.; Olsen, B.; Mitlin, D. ALD TiO_2 Coated Silicon Nanowires for Lithium Ion Battery Anodes with Enhanced Cycling Stability and Coulombic Efficiency. *Phys. Chem. Chem. Phys.* **2013**, *15*, 13646–13657.
28. Pfanzelt, M.; Kubiak, P.; Fleischhammer, M.; Wohlfahrt-Mehrens, M. TiO_2 Rutile—An Alternative Anode Material for Safe Lithium-Ion Batteries. *J. Power Sources* **2011**, *196*, 6815–6821.
29. Belharouak, I.; Sun, Y.-K.; Lu, W.; Amine, K. On the Safety of the $Li_4Ti_5O_{12}$/$LiMn_2O_4$ Lithium-Ion Battery System. *J. Electrochem. Soc.* **2007**, *154*, A1083–A1087.
30. Wu, J.; Wang, N.; Zhao, Y.; Jiang, L. Electrospinning of Multilevel Structured Functional Micro-/Nanofibers and Their Applications. *J. Mater. Chem. A* **2013**, *1*, 7290–7305.
31. Jeong, G.; Lee, S. M.; Choi, N. S.; Kim, Y.-U.; Lee, C. K. Stabilizing Dimensional Changes in Si-Based Composite Electrodes by Controlling the Electrode Porosity: An *In Situ* Electrochemical Dilatometric Study. *Electrochim. Acta* **2011**, *56*, 5095–5101.
32. Hwang, T. H.; Lee, Y. M.; Kong, B.-S.; Seo, J.-S.; Choi, J. W. Electrospun Core–Shell Fibers for Robust Silicon Nanoparticle-Based Lithium Ion Battery Anodes. *Nano Lett.* **2012**, *12*, 802–807.
33. Salam, L. A.; Matthews, R. D.; Robertson, H. Pyrolysis of Poly-methyl Methacrylate (PMMA) Binder in Thermoelectric Green Tapes Made by the Tape Casting Method. *J. Eur. Ceram. Soc.* **2000**, *20*, 335–345.
34. Dong, Y.; Gui, Z.; Jiang, S.; Hu, Y.; Zhou, K. Carbonization of Poly(methyl methacrylate) by Incorporating Hydroxyapatite Nanorods during Thermal Degradation. *Ind. Eng. Chem. Res.* **2011**, *50*, 10903–10909.
35. Lomakin, S. M.; Zaikov, G. E. Pyrolysis and Carbonization of Cross-Linked Poly(methyl methacrylate). *Int. J. Polym. Mater.* **1995**, *27*, 223–230.
36. Ghicov, A.; Tsuchiya, H.; Macak, J. M.; Schmuki, P. Annealing Effects on the Photoresponse of TiO_2 Nanotubes. *Phys. Status Solidi A* **2006**, *203*, R28–R30.
37. Sekiya, T.; Yagisawa, T.; Kamiya, N.; Das Mulmi, D.; Kurita, S.; Murakami, Y.; Kodaira, T. Defects in Anatase TiO_2 Single Crystal Controlled by Heat Treatments. *J. Phys. Soc. Jpn.* **2004**, *73*, 703–710.
38. Tauc, J.; Grigorovici, R.; Vancu, A. Optical Properties and Electronic Structure of Amorphous Germanium. *Phys. Status Solidi B* **1966**, *15*, 627–637.
39. Kofstad, P. Note on the Defect Structure of Rutile (TiO_2). *J. Less-Common Met.* **1967**, *13*, 635–638.
40. The basic material characterization and the electrochemical performance of the SiNPs@C prepared in this study are displayed in the Supporting Information, Figures S8 and S9.
41. Zachau-Christiansen, B.; West, K.; Jacobsen, T.; Atlung, S. Lithium Insertion in Different TiO_2 Modifications. *Solid State Ionics* **1988**, *28–30*, 1176–1182.
42. Gupta, A.; Hartner, S.; Wiggers, H. Optical and Electrical Properties of Silicon Nanoparticles. *3rd International Nanoelectronics Conference* (INEC), **2010**, Hong Kong, pp 616–617.
43. Song, T.; Xia, J.; Lee, J.-H.; Lee, D. H.; Kwon, M.-S.; Choi, J.-M.; Wu, J.; Doo, S. K.; Chang, H.; Park, W. I.; *et al.* Arrays of Sealed Silicon Nanotubes as Anodes for Lithium Ion Batteries. *Nano Lett.* **2010**, *10*, 1710–1716.
44. Yoo, H.; Lee, J.-I.; Kim, H.; Lee, J.-P.; Cho, J.; Park, S. Helical Silicon/Silicon Oxide Core–Shell Anodes Grown onto the Surface of Bulk Silicon. *Nano Lett.* **2011**, *11*, 4324–4328.
45. Chen, Z.; Belharouak, I.; Sun, Y.-K.; Amine, K. Titanium-Based Anode Materials for Safe Lithium-Ion Batteries. *Adv. Funct. Mater.* **2013**, *23*, 959–969.
46. Obrovac, M. N.; Christensen, L. Structural Changes in Silicon Anodes during Lithium Insertion/Extraction. *Electrochem. Solid-State Lett.* **2004**, *7*, A93–A96.
47. Vijayakumar, M.; Kerisit, S.; Wang, C.; Nie, Z.; Rosso, K. M.; Yang, Z.; Graff, G.; Liu, J.; Hu, J. Effect of Chemical Lithium Insertion into Rutile TiO_2 Nanorods. *J. Phys. Chem. C* **2009**, *113*, 14567–14574.
48. Park, C.-M.; Chang, W.-S.; Jung, H.; Kim, J.-H.; Sohn, H.-J. Nanostructured Sn/TiO_2/C Composite as a High-Performance Anode for Li-Ion Batteries. *Electrochem. Commun.* **2009**, *11*, 2165–2168.
49. Tomozeiu, N. Silicon Oxide (SiO_x, $0 < x < 2$): A Challenging Material for Optoelectronics. In *Optoelectronics-Materials and Techniques*; Predeep, P., Ed.; InTech: Rijeka, 2011; pp 55–98.